Research Article

Phase-dependent Electrocatalytic Nitrate Reduction to Ammonia on Janus Cu@Ni Tandem Catalyst

Yao-Yin Lou,* Qi-Zheng Zheng, Shi-Yuan Zhou, Jia-Yi Fang, Ouardia Akdim, Xing-Yu Ding, Rena Oh, Gyeong-Su Park, Xiaoyang Huang,* and Shi-Gang Sun*

Read Online

ACCESS | Metrics & More | Article Recommendations | Supporting Information

ABSTRACT: Electrosynthesis of NH_3 from nitrate anion (NO_3^-) reduction (NO_3^-RR) is a cascade reaction, which is considered a great potential alternative to the Haber−Bosch route to reduce CO_2 emissions and alleviate the adverse effects of excessive NO_3^- contamination in the environment. Frequently, solid solution alloys (SSAs) with a single-phase active site may struggle to fully utilize their benefits during the entire process of nitrate (NO_3^-) reduction, which involves multiple intermediate reactions. In this study, we showed that by separating Cu and Ni in a Janus Cu@Ni catalyst structure, we can achieve high performance in NO_3^-RR, yielding a high Faradaic efficiency (92.5%) and a production rate of NH_3 (1127 mmol h^{-1} g^{-1}) at −0.2 V versus RHE, compared to CuNi SSA (82.6%, 264 mmol h^{-1} g^{-1}). Here, we demonstrate that a Janus Cu@Ni catalyst with short-range ordered catalytic sites favors the adsorption of NO through a bridge-bond mode. Simultaneously, a hydrogen spillover process was observed, in which Ni dissociates H_2O to generate *H which spontaneously migrates to adjacent catalytic sites to hydrogenate the $*NO_x$ intermediates. This facilitates N−O bond cleavage, resulting in the NH_3 production rate nearly 5 times higher than that of CuNi SSA, where NO was linearly bonded on its surface. The study of this catalytic effect, a cooperative tandem enhancement, provides insights into the design of multifunctional heterogeneous catalysts for electrochemical NH_3 synthesis.

KEYWORDS: electrochemical ammonia synthesis, Cu@Ni, phase separation, tandem catalyst, short-range ordered catalytic sites

INTRODUCTION

Catalysts based on bimetallic nanoparticles have received tremendous scientific and industrial investigation and have established themselves as an essential class of active catalysts. Indeed, alloying two metals can dramatically enhance catalytic activity and products selectivity compared to analogous monometallic counterparts.[1] The improved catalytic performances of alloy catalysts are mainly due to the synergic cooperation between the two metals within the bimetallic catalyst through structural and electronic effects.[2,3] Thanks to these two effects, the interactions of reaction intermediates with the catalyst surface can be effectively modulated, significantly influencing the overall reaction activity and selectivity during catalysis. To date, most bimetallic catalysts reported in the literature are solid-solution alloys that contain a single phase. Their properties are usually the weighted average of the different local atomic arrangements. Another kind of bimetallic catalyst is a Janus bimetallic alloy that has a separation of the two metals and is commonly applied for tandem catalysis. Janus alloys with multifunctional active sites with different catalytic properties produce the nanoparticle of a great activity in cascade catalytic reactions,[4] which has always been challenging with the solid-solution alloys (SSAs). However, there has not been an adequate understanding of the unique potential of Janus alloys in catalysis,

although recent studies have revealed that some Janus bimetallic catalysts have better catalytic performances than SSA of the same composition.[5−7]

For the target of attaining net zero carbon by 2050, researchers have been seeking new sustainable technologies to facilitate "greener" and more efficient chemical synthesis routes. The industrial synthesis of NH_3 relies heavily on the Haber−Bosch route,[8] which accounts for roughly 1.2% of global annual CO_2 emissions that surpasses any other industrial chemical-making reactions.[9,10] Electrosynthesis of NH_3 from nitrate anion (NO_3^-) reduction (NO_3^-RR), which could be powered by renewable energy, has been considered as a potential alternative to the Haber−Bosch route.[11] NO_3^- is found extensively throughout both industrial and agricultural wastewater.[12] Not only could electroreduction of NO_3^- from sewage alleviate the adverse effects of excessive NO_3^- contamination in the environment,[13] electrocatalytic production of NH_3 also reduces
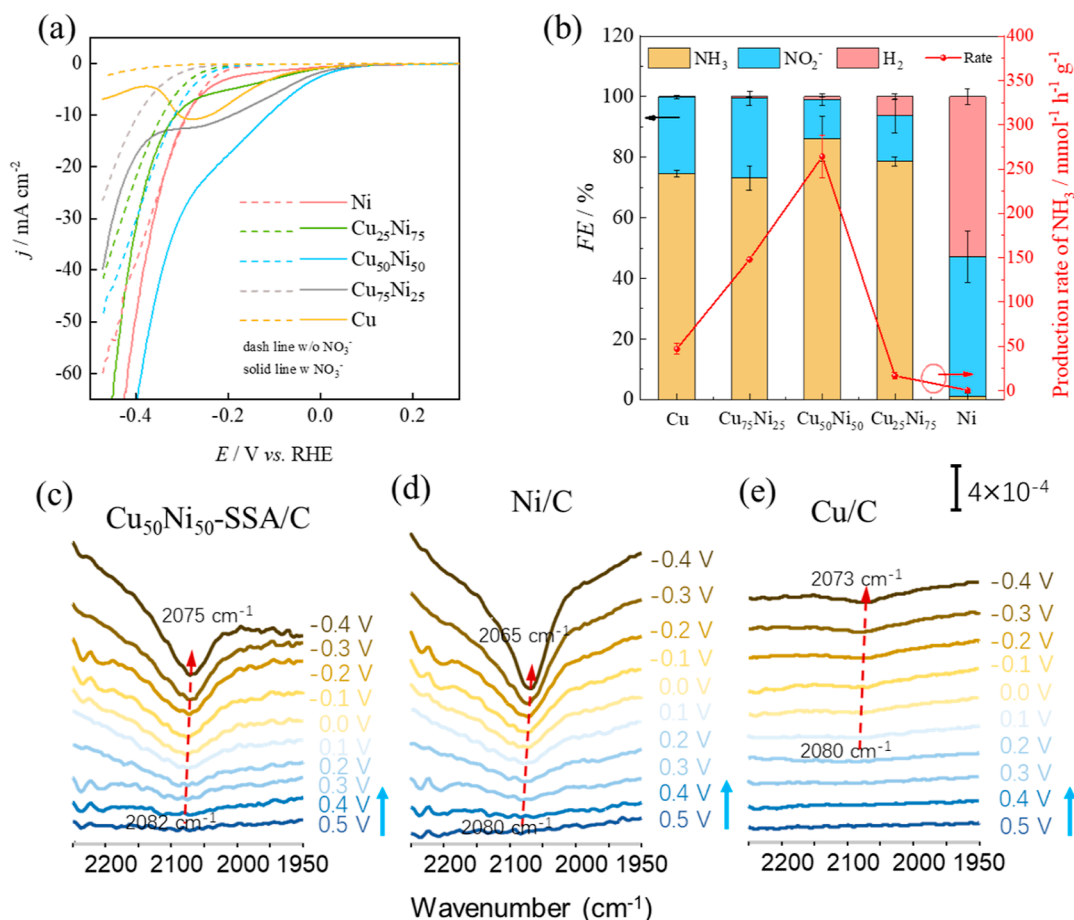
Figure 1. (a) Linear sweep voltammetry of Cu/C, $Cu_{75}Ni_{25}$−SSA/C, $Cu_{50}Ni_{50}$-SSA/C, $Cu_{25}Ni_{75}$−SSA/C, and Ni/C in 1 M KOH with (solid line) and without (dash line) 0.1 M KNO$_3$. Scan rate: 10 mV s^{-1}. (b) Faradaic efficiency of NH$_3$, NO$_2^-$, and H$_2$ (histogram) and production rate of NH$_3$ (line) over Cu/C, $Cu_{75}Ni_{25}$−SSA/C, $Cu_{50}Ni_{50}$-SSA/C, $Cu_{25}Ni_{75}$−SSA/C, and Ni/C at −0.2 V vs RHE. Electrochemical FTIR spectra of $Cu_{50}Ni_{50}$-SSA/C (c), Ni/C (d), and Cu/C (e) in 1 M KOH without KNO$_3$. The associated error bars correspond to the mean ± s.d. (n = 3).

the CO$_2$ emissions, that helps achieve the goal of carbon neutrality. According to some studies,[14,15] NO$_3^-$RR to NH$_3$ is considered as a cascade reaction, involving the transfer of eight electrons and nine protons, where NO$_3^-$ is first reduced into NO$_2^-$, and subsequently further reduced to NH$_3$. Catalyst with a single type of catalytic site (such as SSA) can hardly benefit from their homogeneous alloying structure in the whole NO$_3^-$RR process. In comparison, the Janus catalyst with tandem sites has the capability to modify the adsorption energies of NO$_3^-$RR intermediates by adjusting the electronic structure but also could optimize the reaction pathway. For example, between the Pd(111) and Pd(100) facets over the surface structure of Pd nanoparticles;[16] particles with a core−shell structure containing Cu/CuO$_x$ and Co/CoO phases, respectively.[4] This in turn accelerates the reaction kinetics by leveraging its multifunctional catalytic sites for the relay reactions. Herein, it is with utmost importance to provide an alternative explanation on the mechanism of this reaction over Janus alloy where the catalytic activity may be enhanced. Typically, Cu is considered as one of the best electrocatalysts for NO$_3^-$RR to NH$_3$,[17,18] owing to the similar energy level between d-orbital on it and LUMO π* orbital of NO$_3^-$ resulting in a good affinity for the reduction of NO$_3^-$ as well as its hydrogenated intermediates.[19] However, Cu has a low *H (adsorbed hydrogen) formation ability,[20] which causes the accumulation of NO$_2^-$ intermediates on the surface (i.e., high coverage of nitrogenous species and low coverage of

*H). This effect poisons the active sites and leads to unsatisfactory catalytic activity and low product selectivity over pure Cu. The imbalance between *NO$_x$ and *H adsorption can be a limiting factor.[21,22] To address this issue, researchers have explored Cu-based alloyed catalysts, e.g., Pd−Cu, Co−Cu, Ni−Cu, and Ru−Cu, which have demonstrated enhanced catalytic activities by fine-tuning the adsorption energy of *H and *NO$_x$.[21,23−26] Despite these encouraging progresses, their achievable performances still fall short of expectations due to the cascade reaction system of the NO$_3^-$RR to NH$_3$. Indeed, Cu-based alloyed catalysts can rarely display activity for certain reaction steps of the cascade process. In the present work, we have compared the activity of a classical CuNi SSA/C with a Janus Cu@Ni catalyst supported on XC-72 and a physical mixture of Cu/C and Ni/C. Due to its intrinsic structure, the Janus Cu@Ni catalyst exhibits a high activity (almost 5 times to the current density over alloyed catalyst) across all the reaction steps of the NO$_3^-$RR process. The underlying mechanism over the Janus Cu@Ni catalyst during NO$_3^-$RR is attributed to the cooperative effect observed within its multiphased structure, where the short-range ordered catalytic sites favor the adsorption of NO through a bridge-bond mode. In contrast, the NO intermediate was linearly bonded over the CuNi SSA/C catalyst. All of the investigations in this study were well supported by in situ electrochemical ATR−FTIR and DFT calculations. Our emphasis lies in the investigation of the
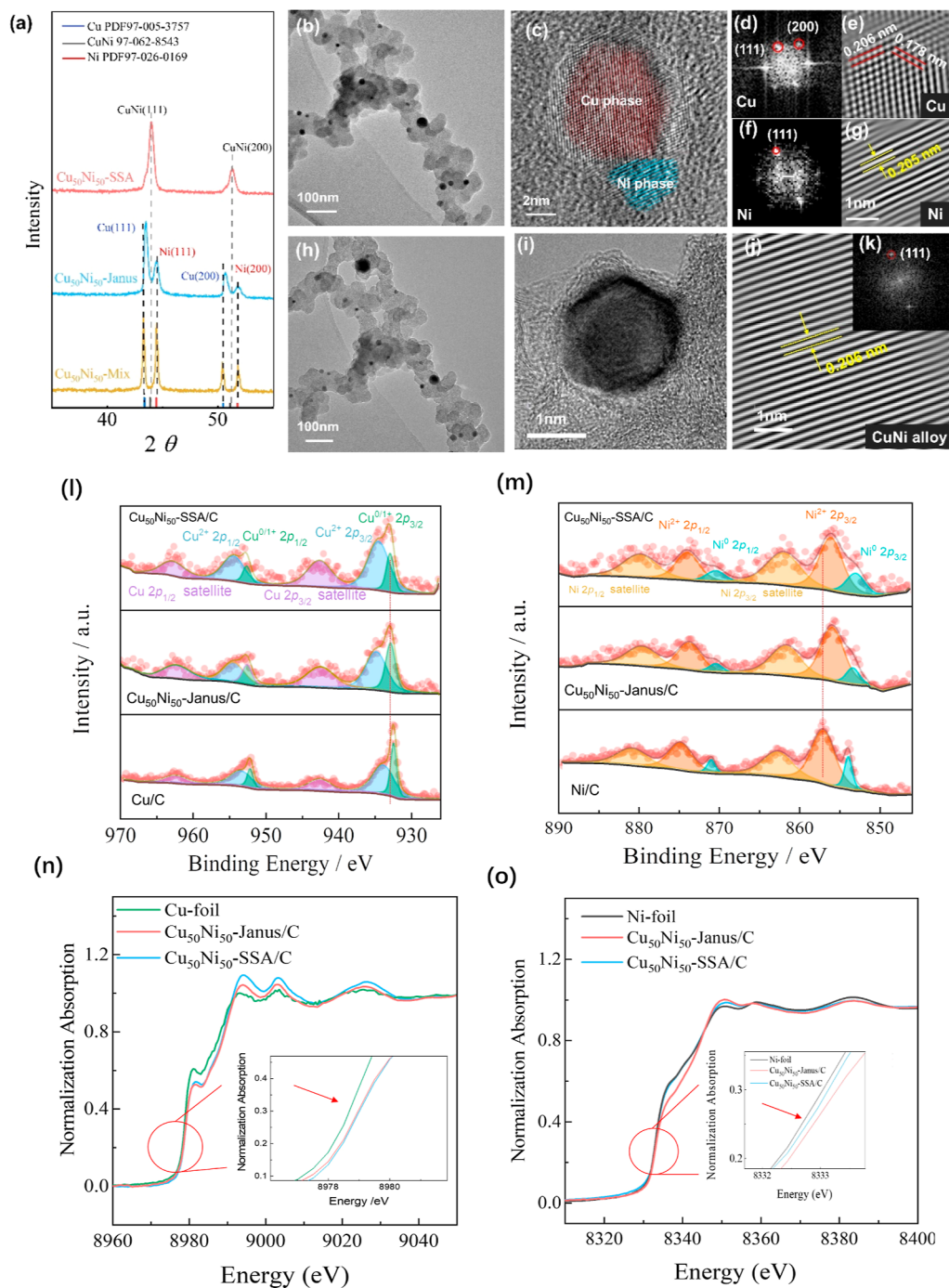
Figure 2. XRD patterns of $Cu_{50}Ni_{50}$-Mix/C, $Cu_{50}Ni_{50}$-Janus/C, and $Cu_{50}Ni_{50}$-SSA (a). TEM image of $Cu_{50}Ni_{50}$-Janus/C (b), HR-TEM image of a single nanoparticle of $Cu_{50}Ni_{50}$-Janus/C (c), and the corresponding FFT diffraction pattern (d,f) and IFFT image (e,g) of the Cu-rich and Ni-rich phase, respectively. TEM image of $Cu_{50}Ni_{50}$-SSA/C (h). HRTEM image of a single nanoparticle of $Cu_{50}Ni_{50}$-SSA/C (i) and the corresponding IFFT image (j) and FFT diffraction pattern (k). XPS spectra of Cu 2p (l) and Ni 2p (m) of $Cu_{50}Ni_{50}$-Janus/C and $Cu_{50}Ni_{50}$-SSA/C, compared to Cu/C and Ni/C. X-ray absorption near edge structure (XANES) spectra of Cu (n) and Ni (o) K-edge of the $Cu_{50}Ni_{50}$-Janus/C, $Cu_{50}Ni_{50}$-SSA/C, and standard samples.

mechanism, highlighting the novelty of metal separation that actively catalyzes the electrochemical reaction. This is an alternative to the widely reported homogeneously alloyed catalysts.

RESULTS AND DISCUSSION

CuNi SSAs supported on XC-72 with Cu/Ni ratios of 25:75, 50:50, and 75:25, along with their monometallic counterparts

were prepared via a simple impregnation method (Supporting Information, Text S1, Table S1 and Figure S1), and their activity was subsequently assessed (Figure 1a). In the absence of nitrate, the highest hydrogen evolution reaction (HER) activity was observed over the monometallic Ni/C displaying the smallest HER Taffel slope, i.e., 87.5 mV dec^{-1} (Supporting Information, Figure S2). This value close to 118 mV dec^{-1} revealed that the Volmer step was the rate-determining step (RDS).[27] In the

presence of 100 mM NO_3^-, the current density (j) increased greatly over all the Cu-based catalysts, notably, the $Cu_{50}Ni_{50}$-SSA/C catalyst showed the highest NO_3^-RR current density than any other catalysts with different metal ratios (Figure 1a). In comparison, a negligible increase of the current density was observed over Ni/C. The NH_3 yield rate (Y_{NH3}) on Cu/C (47.2 mmol^{-1} h^{-1} g^{-1}) was about 118 times higher than that on Ni/C (0.4 mmol^{-1} h^{-1} g^{-1}), see Figure 1b. The addition of Ni to Cu dramatically increased the Y_{NH3}, from 47.2 mmol^{-1} h^{-1} g^{-1} on Cu/C to 264.1 mmol^{-1} h^{-1} g^{-1} on $Cu_{50}Ni_{50}$-SSA/C. Based on these results, it can be inferred that Cu sites serve as the main active site for NO_3^- adsorption during NO_3^-RR while Ni sites play an important role in providing *H via the Volmer step ($H_2O + e^- \rightarrow H^* + OH^-$). When the Ni proportion in the alloy exceeded 50%, a sharp decrease in Y_{NH3} was observed. For example, only about 17 mmol^{-1} h^{-1} g^{-1} of Y_{NH3} was generated on $Cu_{25}Ni_{75}$−SSA/C, and this was ascribed to the ensemble effect caused by the dilution of the Cu sites by Ni atoms' incorporation.[28] In that case, the *H coverage was sufficiently high to prevent the adsorption of NO_3^- over $Cu_{25}Ni_{75}$−SSA/C. The volcano shape of Y_{NH3} substantiated that Cu was the main active sites for NO_3^- adsorption during NO_3^-RR to NH_3. It is evident from this data that an appropriate Cu/Ni ratio plays a crucial role in achieving a balanced coverage of *NO_3^- and *H on the catalytic surface, which is critical to maintaining high catalytic performances in NH_3 production.[21] It is also interesting to note that the Faradaic efficiency of NH_3 (FE_{NH3}) was comparable and between 74 and 86% among Cu-based catalysts, indicating that the introduction of Ni could tune *H coverage but not affect FE_{NH3}.

In situ electrochemical attenuated total reflection FTIR (ATR−FTIR) spectroscopy was used to monitor the signals of *H on the catalysts. A downward peak at 2082 cm^{-1} assigned to the vibration of the bond of *H and a metal surface was observed at 0.3 V versus RHE in 1 M KOH electrolyte free of NO_3^- on $Cu_{50}Ni_{50}$-SSA/C (Figure 1c). The band center was red-shifted to 2075 cm^{-1} at −0.4 V, yielding a Stark turn rate of 10 cm^{-1} V^{-1}. The Stark effect in the vibration frequency indicated the enhanced adsorption of hydrogen atoms on the $Cu_{50}Ni_{50}$-SSA/C surface at higher overpotentials (η) according to eq 1. When the potential negatively shifted, the intensity of *H gradually raised. In that case, the Volmer step was highly promoted, and therefore, more *H were generated, which in turn enhanced the hydrodeoxidation reaction and gave a higher $\frac{NH_3}{NO_2^- + NH_3}$ ratio (Supporting Information, Figure S3). The fact that *H signals on $Cu_{50}Ni_{50}$-SSA/C and Ni/C were much stronger than that over Cu (appearing potential was positively shifted by 200 mV), Figure 1d,e, gave strong evidence that *H on CuNi bimetallic catalysts was mainly attributed to water dissociation on Ni sites. With the addition of NO_3^-, the peak intensity from *H decreased on $Cu_{50}Ni_{50}$-SSA/C (Supporting Information, Figure S4a) due to the competitive adsorption of *NO_3^- with *H on the catalytic surface. In the Cu/C spectra, *H vanished (Supporting Information, Figure S4b), while the Ni/C surface maintained the *H signal (Figure S4c), reaffirming that Cu and Ni sites were responsible for NO_3^- and H adsorption, respectively. Electron paramagnetic resonance (EPR) spectroscopy was conducted to detect the presence of *H (Supporting Information Figure S5) using 5,5-dimethyl-1-pyrroline N-oxide (DMPO) as a spin trap.[29] In the presence of nitrate, the intensity of the EPR signal of the DMPO-*H adduct on $Cu_{50}Ni_{50}$-SSA/C

decreased. These results align consistently with the ATR−FTIR analysis.

$$\eta = E - E_{eq} = \frac{RT}{F}\ln\frac{\theta_H}{\theta_H^0} \tag{1}$$

Where θ_H and θ_H^0 are the *H coverage at E and E°, respectively; F is the Faraday constant, 96485 C mol^{-1}; R is the gas constant, 8.314 J mol^{-1} K^{-1}; and T is the kelvin temperature, K.

While CuNi catalysts with other ratios and their physical structures remain of importance, we opted to primarily focus on the Cu/Ni ratio of 50:50 which showed the highest activity in the NO_3^-RR (Figure 1a). To gain insights into this behavior, we prepared two other samples with the same 50:50 ratio. These samples include the XC-72 supported Cu@Ni Janus alloy (referred to as $Cu_{50}Ni_{50}$-Janus/C, Figure 2) and a physical mixture of Cu/C and Ni/C catalysts (denoted as $Cu_{50}Ni_{50}$-Mix/C). The preparation for $Cu_{50}Ni_{50}$-Janus/C followed the same step as that of the $Cu_{50}Ni_{50}$-SSA/C synthesis (700 °C), with the exception that the annealing temperature was set at 500 °C. TEM-EDS mapping of $Cu_{50}Ni_{50}$-Janus/C and $Cu_{50}Ni_{50}$-SSA/C revealed a uniform distribution of Cu and Ni on the carbon substrate (Supporting Information, Figure S6). The average particle size was similar for both catalysts, measuring 22.2 ± 11.1 and 23.6 ± 10.8 nm, respectively (Supporting Information, Figure S7a,b). The XRD pattern of $Cu_{50}Ni_{50}$-SSA/C (PDF #062−8543) displayed two peaks assigned to a pure alloy. The peak fitting and refinement of the main peak of $Cu_{50}Ni_{50}$-SSA/C were performed (Supporting Information, Figure S7c). There were two subpeaks obtained at 43.4 and 44.0°, which were accounted for 9.9 and 91% of the peak area. The main subpeak at 44.0° was assigned to CuNi(111) and the minor subpeak at 43.4° was should ascribed to Cu(111) at 42.3° that was incorporated by Ni atoms. The XRD pattern of $Cu_{50}Ni_{50}$-Janus/C confirmed the separation of Cu and Ni, by exhibiting two sets of diffraction peaks assigned to a typical face-centered cubic (fcc) structure for Cu (PDF #005−3757) and Ni (PDF #026−0169) (Figure 2a), respectively, and was similar to the pattern of $Cu_{50}Ni_{50}$-Mix/C. The two sets of diffraction peaks of $Cu_{50}Ni_{50}$-Janus/C showed a convergence toward each other, indicating that $Cu_{50}Ni_{50}$-Janus/C had a Janus structure with coexisting Cu-rich and Ni-rich solid solutions. The Janus structure was also confirmed by the HR-TEM image of a single nanoparticle (Figure 2b,c) with the assistance of Fourier transform (FFT)/inverse Fourier transform (IFFT) images (Figure 2d−g). The lattice spacing constriction observed on the Cu phase, as compared to the PDF standard card for fcc Cu (PDF #005−3757), further indicates the incorporation of some Ni atoms within the Cu lattice. In parallel, the same phenomenon was observed with Ni, indicating the incorporation of some Cu atoms in its lattice. In the case of $Cu_{50}Ni_{50}$-SSA/C, the HR-TEM and corresponding FFT/IFFT images displayed a homogeneous distribution of Cu and Ni within the nanoparticle with a one-phase structure, supporting the existence of a CuNi alloy phase (Figure 2h−k). The extended X-ray absorption fine structure (EXAFS) analysis further confirmed the coordination structures of those two CuNi bimetallic alloys (Supporting Information, Figure S8). The Fourier transform (FT) K$_3$-weighted EXAFS spectra exhibited a metal interaction peak around 2.2 Å, indicating the main formation of metallic bonds. The structural parameters of Cu and Ni atoms were also obtained and are summarized in Supporting Information, Table S2. In $Cu_{50}Ni_{50}$-

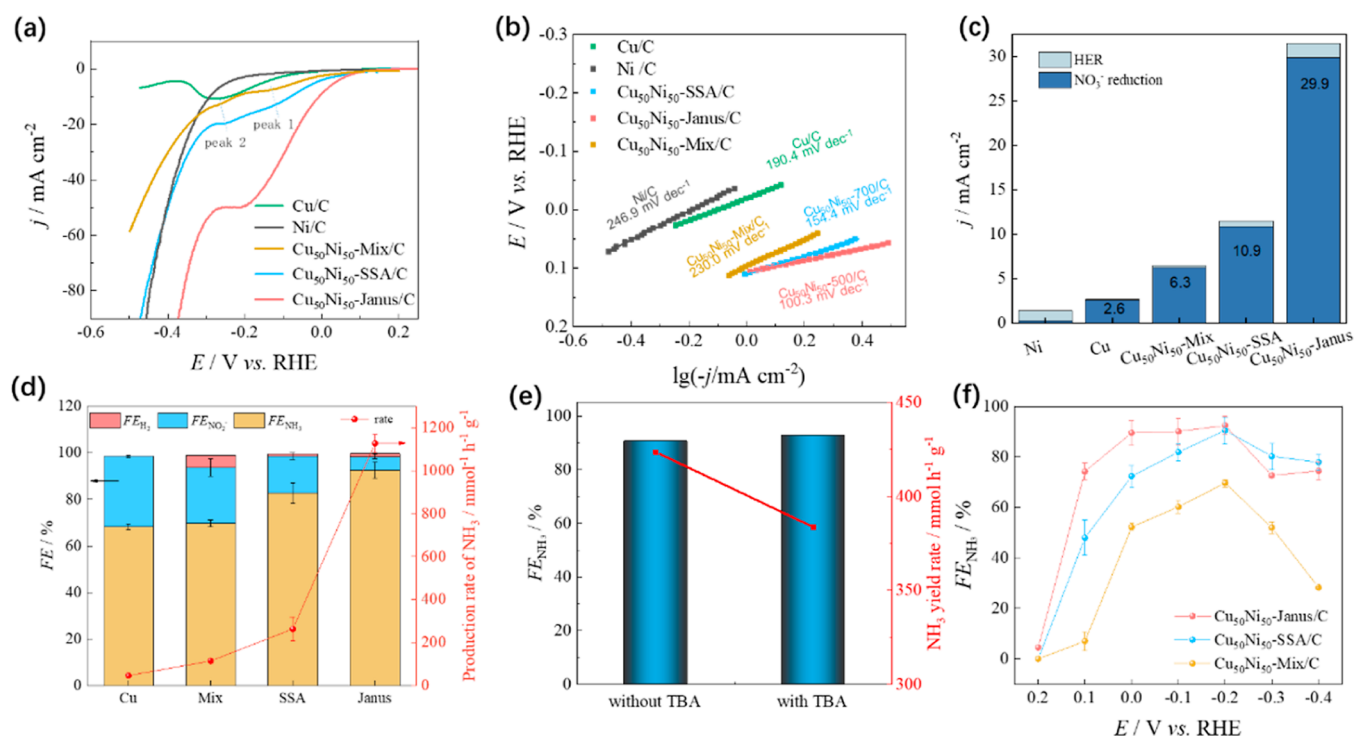**Figure 3.** j-E curve (80% iR corrected) over $Cu_{50}Ni_{50}$-Janus/C, $Cu_{50}Ni_{50}$-SSA/C, $Cu_{50}Ni_{50}$-Mix/C, and Cu/C and Ni/C modified rotate disk electrode (catalysts loading was 0.2 mg cm^{-2}) in 1 M KOH solution containing 100 mM KNO$_3$ at a scan rate of 10 mV s^{-1} with the rotate rate as 900 rpm (a). Tafel slopes (b). According to the results from (a) Bias current density of NO$_3^-$RR and HER according to (c). FE and Y_{NH_3} over $Cu_{50}Ni_{50}$-Janus/C-, $Cu_{50}Ni_{50}$-SSA/C-, $Cu_{50}Ni_{50}$-Mix/C-, Cu/C-, and Ni/C-coated carbon cloth (5 mg cm^{-2}) at −0.2 V vs RHE in 1 M KOH solution containing 100 mM KNO$_3$ (d). FE_{NH3} and Y_{NH3} over $Cu_{50}Ni_{50}$-SSA/C-coated carbon cloth (5 mg cm^{-2}) at −0.2 V vs RHE in 1 M KOH solution containing 100 mM KNO$_3$ with and without TBA addition (50 mM) (e). FE_{NH3} over $Cu_{50}Ni_{50}$-Janus/C, $Cu_{50}Ni_{50}$-SSA/C, $Cu_{50}Ni_{50}$-Mix/C, Cu/C, and Ni/C coated on carbon cloth (5 mg cm^{-2}) in the potential window from 0.2 to −0.4 V vs RHE (f). The associated error bars correspond to mean ± s.d. (n = 3).
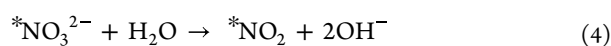
Janus/C, each Cu atom is coordinated by an average of approximately 10.8 Cu and 1.2 Ni atoms, while each Ni atom is coordinated by an average of 10.8 Ni and 1.2 Cu atoms. This observation supports the preservation of a short-range ordered structure in both the Cu-rich and Ni-rich phases. On the other hand, in $Cu_{50}Ni_{50}$-SSA/C, Cu and Ni atoms were each coordinated by six Cu and six Ni atoms, respectively, confirming its solid solution alloy structure with a uniform 1:1 mixture of Cu and Ni.

The electronic structure of $Cu_{50}Ni_{50}$-SSA/C and $Cu_{50}Ni_{50}$-Janus/C was further studied, given that the alloying degree of Ni with Cu can tune the electronic structure of the catalysts.[30] The XPS results revealed high-intensity signals for Cu^{2+} 2p and Ni^{2+} 2p on Cu/C, Ni/C, and bimetallic catalysts due to the oxidation of metallic sites resulting from the exposition of the catalyst to air (Figure 2l,m). In addition, compared with the Cu/C catalyst, the Cu$^{0/1+}$ 2$p_{3/2}$ peak of the alloy catalyst shifted toward a lower binding energy. Similarly, compared with the Ni/C catalyst, the Ni^{2+} 2$p_{3/2}$ peak of the alloy catalyst shifted toward a higher binding energy, indicating a redistribution of electrons among Cu and Ni atoms within their alloyed structure. These results aligned consistently with XANES characterization (Figure 2n,o). The Ni K-edge of CuNi bimetals showed a slight positive shift as compared with the Ni reference, which demonstrated an increase in the Ni valence state of $Cu_{50}Ni_{50}$-Janus/C and $Cu_{50}Ni_{50}$-SSA/C. The Cu K-edge of the CuNi bimetals also showed a positive shift toward a higher energy than that of the Cu reference, which could be ascribed to the oxidation of Cu when being exposed to air. In addition, according to the Bader charge analysis, a charge redistribution on CuNi(111) was

observed in comparison to monometallic Cu and Ni; within this redistribution, the Ni center displayed an increased Bader charge, while the Cu center showed a decreased Bader charge (Supporting Information, Figure S9). Furthermore, the impedance of $Cu_{50}Ni_{50}$-Mix/C (74.1 Ω) was significantly higher than that of the CuNi alloy catalyst (46.3 Ω for $Cu_{50}Ni_{50}$-SSA/C and 48.2 Ω for $Cu_{50}Ni_{50}$-Janus/C), Supporting Information, Figure S10. The electrons redistribution between Cu and Ni atoms plays an important role in modulating the adsorption energy of the *NO$_3^-$, and reducing intermediate species and *H.[30] The electrocatalytic activities of $Cu_{50}Ni_{50}$-Janus/C, $Cu_{50}Ni_{50}$-SSA/C, and $Cu_{50}Ni_{50}$-Mix/C toward NO$_3^-$RR, in comparison to Cu/C and Ni/C were then evaluated.

First, the linear sweep voltammograms (LSVs) were performed in Ar-saturated solutions of 1 M KOH +100 mM KNO$_3$ (Figure 3a). Two reduction current peaks (Peaks 1 and 2) appeared in the Cu-based catalysts' curves. According to previous studies,[31,32] the Peak 1 near −0.1 V versus RHE was assigned to the reduction of *NO$_3^-$ (adsorbed NO$_3^-$) into *NO$_2^-$ following a two-electron transfer process (*NO$_3^-$ + 2e$^-$ + H$_2$O → *NO$_2^-$ + 2OH$^-$), while the Peak 2 was mainly attributed to the *NO$_2^-$ reduction into *NH$_3$ following a six-electron transfer process (*NO$_2^-$ + 6e$^-$ + 5H$_2$O → *NH$_3$ + 7OH$^-$). The Tafel curves were fitted and the obtained Tafel slopes were close to or greater than 118 mV dec^{-1} on all the catalysts (Figure 3b), indicating that the rate-determinate step (RDS) was the electron transfer during *NO$_3^-$ to *NO$_2^-$ step, (eqs 2−5).[33] According to the Tafel slopes and bias current density of NO$_3^-$ reduction ($j_{NO_3^-}$), $Cu_{50}Ni_{50}$-Janus/C (100 mV dec^{-1}, 30 mA cm^{-2} at −0.1 V), and $Cu_{50}Ni_{50}$-SSA/C (154.4 mV dec^{-1}, 11 mA cm^{-2} at −0.1

V) had an obviously higher kinetic activity for $*NO_3^-$ to $*NO_2^-$ step the $Cu_{50}Ni_{50}$-Mix/C (230 mV dec^{-1}, 6 mA cm^{-2} at −0.1 V). This is due to the redistribution of electrons within the alloy, as evidenced by XPS results and Bader charge analysis, which facilitates the transfer of electrons from the catalyst to $*NO_3^-$ and promotes the RDS. Although the number of Cu sites on $Cu_{50}Ni_{50}$-Mix/C was half of the Cu/C, the $j_{NO_3^-}$ over $Cu_{50}Ni_{50}$-Mix/C was nearly 3 times higher than that of Cu/C (Figure 3c). Furthermore, the current density of NO_3^-RR using $Cu_{50}Ni_{50}$-Mix (6.3 mA.cm^{-2}) was approximately 2.3 times higher than the additive contribution from Ni and Cu (2.6 + 0.1 = 2.7 mA cm^{-2}), where it demonstrates an effect of 1 + 1 > 2 in electrochemical ammonia synthesis. The higher $j_{NO_3^-}$ of $Cu_{50}Ni_{50}$-Mix/C can be attributed to a strong synergy between Cu and Ni in both Janus type and physical mixture configurations, the efficient generation of *H on the Ni/C, which subsequently spills over to the Cu/C surface, thereby promoting the hydrodeoxidation of $*NO_3^-$ species. The gaseous and liquid products after 1 h electrolysis at −0.2 V were collected, and the results are displayed in Figure 3d. NH_3 species were the primary products observed on the Cu-based catalysts. The Y_{NH3} over $Cu_{50}Ni_{50}$-Mix/C was almost 2.5 times higher than that of Cu/C at −0.2 V, demonstrating the effect of hydrogen spillover from Ni sites to Cu sites. Comparable NH_3 selectivity was observed on both $Cu_{50}Ni_{50}$-Mix/C and Cu/C, revealing that the presence of *H mainly contributed to the increased Y_{NH3}. This could be further substantiated using a *H scavenger such as tert-butanol (TBA) which resulted in a decrease in Y_{NH3} from 424 to 380 mmol h^{-1} g^{-1}. However, the FE_{NH3} remained stable at approximately 91% on $Cu_{50}Ni_{50}$-SSA/C (Figure 3e). $Cu_{50}Ni_{50}$-Janus/C demonstrated the utmost efficiency in NH_3 production, as evidenced by the highest FE_{NH3} and the highest Y_{NH3}, reaching, respectively, 92.5% and 1127 mmol h^{-1} g^{-1} at −0.2 V (Figure 3f). The current density for NH3 formation in the solution in the presence of NO_3^- ions is over 145-fold higher than in its absence, where the trace amount of NH3 might come from the N2 reduction. Hence, the N2 reduction reaction has little effect on the quantification of NH3 produced by NO_3^-RR. The NH_3 production rate was also higher than that of the state-of-the-art catalysts reported in the literature (Supporting Information, Figure S11 and Table S3). In comparison, $Cu_{50}Ni_{50}$-SSA/C achieved a FE_{NH3} of 82.6% and a Y_{NH3} of 264 mmol h^{-1} g^{-1}; $Cu_{50}Ni_{50}$-Mix/C achieved a FE_{NH3} of 69.7% and a Y_{NH3} of 115 mmol h^{-1} g^{-1}. Most importantly, $Cu_{50}Ni_{50}$-Janus/C maintained a FE_{NH3} over 90% from 0 V to −0.2 V. The concentrations of Cu^{2+} and Ni^{2+} ions in the electrolyte after 2 h electrolysis at −0.2 V versus RHE values were also determined by ICP−MS. There were about 0.015 mg L^{-1} Cu^{2+} ions and 0.01 mg L^{-1} Ni^{2+} ions detected in the final solutions, which was much lower than the limitations for discharge of heavy metals (GB5759−5005). The concentration of NO_3^- in real wastewater can vary from 1 mmol L^{-1} to 2 mol L^{-1}.[33] Therefore, NO_3^-RR on the Janus catalyst was performed at a wide range of NO_3^- concentrations (1−100 mmol L^{-1}) in neutral media. The FE_{NH3} was maintained above 85% in the whole range of NO_3^- concentrations at −0.2 V. These results demonstrated the excellent property of Janus catalysts toward NO_3^- recovery in various environmental wastewater systems.

$$NO_3^- + * \rightarrow *NO_3^- \qquad (2)$$

$$*NO_3^- + e^- \rightarrow *NO_3^{2-} (RDS) \qquad (3)$$

$$*NO_3^{2-} + H_2O \rightarrow *NO_2 + 2OH^- \qquad (4)$$

$$*NO_2 + e^- \rightarrow *NO_2^- \qquad (5)$$

To gain a better understanding of the role of *H in the steps of NO_3^- reduction to NH_3, we investigated the catalytic activities of NO_2^-RR and NORR. This is significant because NO_2^- and NO are key intermediates in the NO_3^- reduction to NH_3 process.[14,34] At the onset potential of the NO_2^-RR around 0 V, the *H coverage was low since the HER did not occur over any of the studied catalysts (Supporting Information, Figure S12a). Ni/C had the largest Tafel slope of 168.5 mV dec^{-1} for the NO_2^-RR at 0 V (Supporting Information, Figure S12b), indicating a very low catalytic activity of the NO_2^-RR over Ni when the *H coverage was small. When the potential went to −0.2 V, where the HER was enhanced, it leads to a higher *H coverage, and an enhanced $j_{NO_2^-}$ (4.6 mA cm^{-2}) over Ni/C surpassing even the performance of Cu (2.9 mA cm^{-2}), Supporting Information, Figure S12c. Indeed, according to the product analysis, Ni/C has a higher Y_{NH3} (235 mmol h^{-1} g^{-1}) and FE_{NH3} (100%) than Cu (154 mmol h^{-1} g^{-1}, 89%), Supporting Information, Figure S12d. This phenomenon contrasts with the case of the NO_3^- reduction. A scavenger test was also performed on Ni/C during the NO_2^- reduction. After adding TBA, Y_{NH3} on Ni/C decreased from 235 to 123 mmol^{-1} h^{-1} g^{-1} but FE_{NH3} remained around 100%, Supporting Information, Figure S12e. This demonstrates that the *H on the surface primarily enhances the Y_{NH3} rather than FE_{NH3} during the NO_2^-RR. Similar behaviors were observed for the NORR on all of the catalysts (Supporting Information, Figure S13). According to the above discussion, it could be rationally inferred that the reduction of NO_3^- to NO_2^- is limited by electronic transfer within the bimetallic catalyst which could impact the FE_{NH3}. In contrast, *H plays a significant role in the reduction of NO_2^- to NH_3 and mainly affects the Y_{NH3}. The electrochemically active surface area (ECSA) was obtained according to the electrochemical double-layer capacitance determination (Figure S14a−c). The normalized LSV of $Cu_{50}Ni_{50}$-SSA and $Cu_{50}Ni_{50}$-Janus was then presented and a higher $j_{(ECSA)}$ was observed on $Cu_{50}Ni_{50}$-Janus than $Cu_{50}Ni_{50}$-SSA (Figure S14d). The above results demonstrated that $Cu_{50}Ni_{50}$-Janus had a higher intrinsic activity than the $Cu_{50}Ni_{50}$-SSA. The electronic and composition properties of the $Cu_{50}Ni_{50}$-Janus/C post reaction were analyzed by XPS and XRD (Supporting Information, Figures S15 and S16). After electrolysis, the electronic structure and composition were well preserved.

So far, our results indicate that the catalytic activities of NO_3^-RR, NO_2^-RR, and NORR over $Cu_{50}Ni_{50}$-Janus/C were significantly higher than that on $Cu_{50}Ni_{50}$-SSA/C, revealing that the NO_3^-RR, NO_2^-RR, and NORR were phase-dependent reactions on CuNi bimetallic catalysts. This effect is associated with the surface coordination number between active-metal atoms.[28] Compared to $Cu_{50}Ni_{50}$-SSA/C which features a homogeneous mixture of Cu and Ni atoms, $Cu_{50}Ni_{50}$-Janus/C exhibited the formation of a greater number of short-range ordered active sites. In particular, nitrogenous species can form various associations with metallic catalytic surfaces. For instance, the adsorption of NO_x on a catalyst surface may involve conformational variations, encompassing the N-bound nitro, O-bound nitrito, doubly O-bound chelating nitrito, as well as N- and O-bound bridging nitro modes of association. Therefore, it is anticipated that $Cu_{50}Ni_{50}$-Janus/C with a short-range

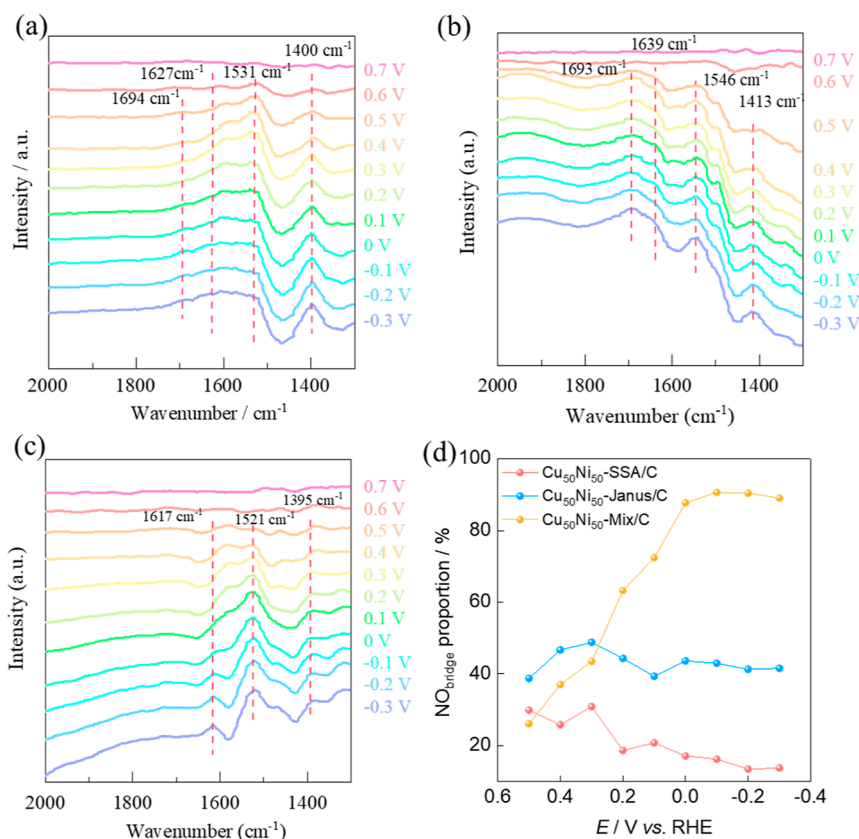**Figure 4.** In situ electrochemical ATR-FTIR spectra of NO reduction on $Cu_{50}Ni_{50}$-SSA/C (a), $Cu_{50}Ni_{50}$-Janus/C (b), and $Cu_{50}Ni_{50}$-Mix/C (c) in 1 M KOH. (d) NO_{bridge} proportion on $Cu_{50}Ni_{50}$-SSA/C, $Cu_{50}Ni_{50}$-Janus/C, and $Cu_{50}Ni_{50}$-Mix/C.
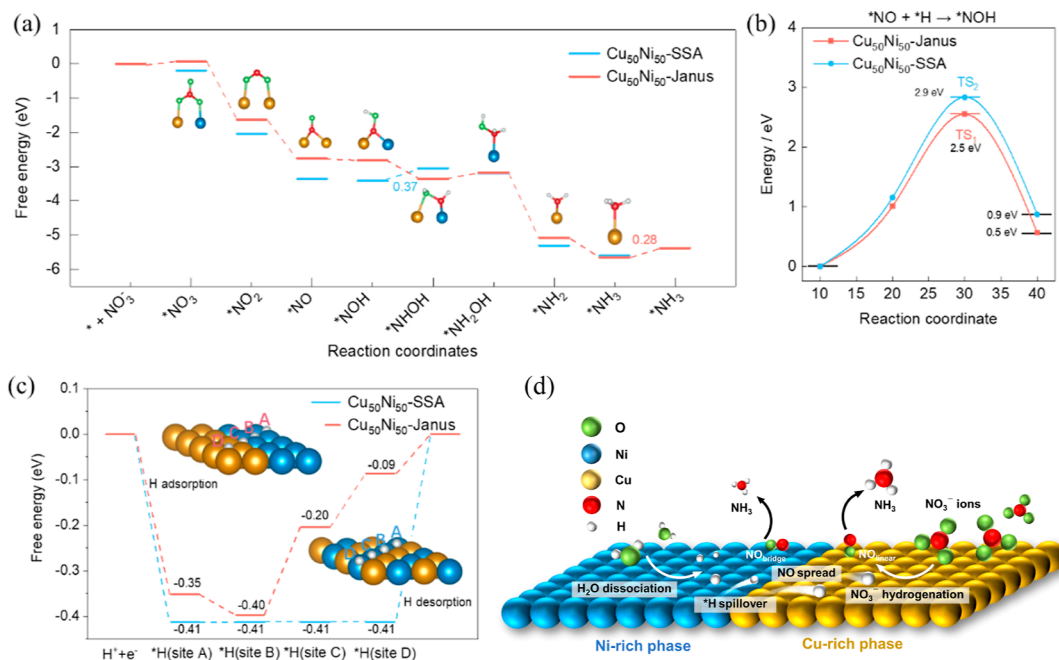

Figure 5. Gibbs free energy diagram of the intermediates generated during electrocatalytic NO_3^-RR over pure CuNi-SSA and CuNi-Janus (a). The structural models represent the adsorption form of various intermediates on CuNi-Janus during NO_3^-RR, Cu yellow, Ni blue, N red, O green, and H light gray atoms. The reaction energy barrier of elementary step $*NO+*H \rightarrow *NOH$ (b). Free energy change of $*H$ at different positions on CuNi bimetallics [top right inset, top view of the atomic CuNi-SSA and CuNi-Janus structure model and labeled $*H$ spillover path ($A \rightarrow B \rightarrow C \rightarrow D$)] (c). Schematic of the reaction mechanism of the enhanced NO_3^-RR process over $Cu_{50}Ni_{50}$-Janus/C (d).

structure could promote the adsorption of nitrogenous species on the catalytic surface.

In the aim to elucidate the preferential adsorption and reduction capabilities of the catalysts for NO, a key intermediate

species in the reaction, in situ electrochemical ATR–FTIR was employed (Figure 4a–d). For all the catalysts as the potential decreases from 0.7 V to −0.3 V, an absorption peak appeared around 1400 cm^{-1} and was ascribed to the N–H stretching.[35] In addition to this peak, a broad band between 1450 and 1800 cm^{-1} was also observed. Deconvoluting this band on the spectra obtained at −0.1 V on $Cu_{50}Ni_{50}$-SSA/C (Figure 4a) unfolded three distinct bands centered at 1712, 1620, and 1531 cm^{-1} (Supporting Information, Figure S17). These bands were attributed to three different adsorption modes of the NO species onto a metal surface, *viz.*: (1) At 0.6 V, a bipolar band of a linearly on-top bonded NO (NO_{linear}) can be observed at 1655–1595 cm^{-1}.[36–39] The bipolar shape can be attributed to the electrode potential's effect on the N–O stretching frequency,[36] resulting in a downward shift of the adsorbate band as the electrode potential decreases. At lower potentials (below 0.2 V), the band transitions to an upward shape due to the NO reduction; (2) simultaneously, at a lower wavelength, around 1531 cm^{-1}, another band appeared and was assigned to N–O stretching of a bridge-bonded NO (NO_{bridge});[38–42] (3) the third band at ca. 1712 cm^{-1} was attributed to the bisnitrosyl adducts of Ni adlayer [$Ni(NO)_2$].[43] The integrated intensities of the three bands versus applied potential were subsequently plotted on the basis of curve fitting, as shown in Supporting Information, Figure S18. The proportion of NO_{bridge} was calculated using eq (S1) and compared among $Cu_{50}Ni_{50}$-Mix/C, $Cu_{50}Ni_{50}$-Janus/C, and $Cu_{50}Ni_{50}$-SSA/C (Figure 4d). $Cu_{50}Ni_{50}$-Mix/C and $Cu_{50}Ni_{50}$-Janus/C exhibited a higher proportion of NO_{bridge} species on their surface in comparison to $Cu_{50}Ni_{50}$-SSA/C. This observation suggests that short-range ordered active sites facilitate the bridge-bonded adsorption of NO, whereas the linear-bonded adsorption configuration predominates on $Cu_{50}Ni_{50}$-SSA/C. Meanwhile, the absorption intensity of N–O stretching was significantly greater on Ni/C in comparison to Cu/C (Supporting Information, Figures S19a–c), indicating that Ni sites accommodate a stronger adsorption affinity for NO. These results align well with DFT calculations, where the Gibbs free energy for NO adsorption on Ni atoms (−2.1 eV) was considerably lower than that on Cu atoms (−1.2 eV). Besides, NO_{bridge} displayed a higher intensity than NO_{linear} on Ni/C, while the NO_{linear} intensity was more pronounced on Cu/C (Supporting Information, Figure S19c,d). This indicates a preference for bridge-bonded and linear-bonded NO adsorption on Ni and Cu atoms, respectively. The much higher intensity of NO peaks (including linear- and bridge- bonded NO) proved that the NO formed from *NO_2 reduction on the Cu-rich phase spilled over to the Ni-rich phase with a bridge-bonded adsorption (Supporting Information, Figures S16). These results provide a robust explanation for the superior catalytic performance of Ni/C over Cu/C during NO_2^-RR and NORR. Moreover, it suggests that during the hydrogenation of the intermediates *NO_2 and *NO, the Ni sites in $Cu_{50}Ni_{50}$-Janus/C serve not only as providers of *H but also as active catalytic sites for NO adsorption.

Figure 5 provides the Gibbs free energies (ΔG) of *NO_3 species and their derivates on $Cu_{50}Ni_{50}$-SSA/C and $Cu_{50}Ni_{50}$-Janus/C based on density functional theory (DFT) calculations. On the basis of the thermodynamics data, the RDS on $Cu_{50}Ni_{50}$-SSA/C was the hydrogenation of *NOH to *NHOH (0.37 eV), Figure 5a. This step on $Cu_{50}Ni_{50}$-Janus/C became spontaneous (−0.54 eV) due to enhanced NO_x adsorption in a bridge-bonded configuration. This result highlights the preference for the hydrogenation of bridge-bonded NO_x into NH_3 on

$Cu_{50}Ni_{50}$-Janus/C. Indeed, it is well acknowledged that NO_{bridge} will cleave more readily than NO_{linear}, to produce NH_3.[37] Besides, the RDS on $Cu_{50}Ni_{50}$-Janus/C became the desorption of *NH_3 with a ΔG of 0.28 eV that was also lower than the ΔG of the RDS on $Cu_{50}Ni_{50}$-SSA/C (0.37 eV). The Gibbs free energies of *NO_3 and *H on Ni and Cu were subsequently compared. Although the adsorption of *NO_3 on Ni (−0.06 eV) was easier than on Cu (0.18 eV) (Figure 5a), the adsorption of *H (−0.32 eV) on Ni was much easier than that of *NO_3 and also easier than *H on the Cu site (−0.18 eV), Supporting Information, Figure S20, which suggests that *H will adsorb preferentially on Ni sites on the CuNi bimetallic catalysts. It was also well fitted with the electrochemical in situ FTIR results that the *H signal was observed on Ni/C but vanished on Cu/C in the presence of NO_3^-. The calculated results also provide an explanation for the relative inertness of monometallic Ni/C toward the NO_3^-RR, as they reveal that the *H coverage on Ni sites is sufficiently high to hinder the adsorption of *NO_3. These theoretical results substantiate the results obtained from in situ electrochemical ATR-FTIR analysis (Figure 1c–e). Additional DFT calculations were performed to elucidate the migration and interaction of *H generated on the Ni sites with the reaction intermediates on the Cu sites. According to the preceding experimental results, the formation of adsorbed *H was crucial for NO_x hydrogenation, and the Gibbs free energy for H adsorption (ΔG_H) emerged as a significant descriptor for the hydrogenation process. Hydrogen spillover usually exists in binary composite materials, with one site (denoted as A) featuring a negative ΔG_H value ($\Delta G_{H(1)}$) and thus a strong H adsorption (such as Ni in this work), and the other site (denoted as D) featuring a positive ΔG_H value ($\Delta G_{H(2)}$) and thus for efficient desorption and further hydrogenation process (such as Cu).[44] Figure 5c provides a summary of the ΔG_H values on various sites within the two theoretical models, $Cu_{50}Ni_{50}$-Janus/C and $Cu_{50}Ni_{50}$-SSA/C, and suggests an energetically favorable *H-spillover process over the Janus-type catalyst. For $Cu_{50}Ni_{50}$-SSA/C, the *H spillover was more inclined to occur on Ni sites and the ΔG_H values remained relatively constant from site A to site D, around −0.41 eV. The Gibbs free energy of *H desorption from site D was as high as 0.41 eV. In contrast, for $Cu_{50}Ni_{50}$-Janus/C, the ΔG_H values are −0.35 eV (site A in Ni-rich phase); −0.44 eV (site B in Ni-rich phase); −0.20 eV (site C in Cu-rich phase); and −0.09 eV (site D in Cu-rich phase), and the Gibbs free energy of *H desorption is significantly lower (0.09 eV). We conducted an analysis of the energy change for hydrogenation process (*NO → *NOH) (Figure 5b) and find that the activation barrier and reaction energy of the hydrogenation on $Cu_{50}Ni_{50}$-Janus/C (2.5 and 0.5 eV respectively) were lower than that on $Cu_{50}Ni_{50}$-SSA/C (2.8 and 0.9 eV), suggesting that hydrogen spillover and bridge-bond NO on $Cu_{50}Ni_{50}$-Janus/C were energetically more favorable for intermediates hydrogenation process, which gave a dramatic leap of the Y_{NH_3} on $Cu_{50}Ni_{50}$-Janus/C (1127 mmol^{-1} h^{-1} g^{-1}) compared to that on $Cu_{50}Ni_{50}$-SSA/C (264 mmol^{-1} h^{-1} g^{-1}).

Drawing from the comprehensive results obtained through in situ electrochemical ATR–FTIR analysis and DFT calculations, we are able to put forth a proposed reaction mechanism for NO_3^-RR on $Cu_{50}Ni_{50}$-Janus/C. This mechanism is illustrated in Figure 5d. Initially, the electron distribution within Janus Cu@Ni structure favors the activation of NO_3^- to form *NO_2 species on the Cu-rich phase and *H generation through Volmer step on the Ni-rich phase, respectively. During the *H-spillover process, the generated *H on Ni spontaneously migrates and

accumulates at the Cu@Ni interface.[45,46] Simultaneously, *NO$_2$ would desorb from Cu atoms and would readsorb onto either Ni or Cu atoms, where the NO$_{bridge}$ and NO$_{linear}$ intermediates were formed, respectively. The NO bridge adsorption would then promote cleavage of the N−O bond. Additional hydrogen-bond interactions between spillover *H and intermediates lead to the desorption of spillover *H from the Cu@Ni interface, enabling it to directly participate in the hydrogenation of bridge-bonded intermediates. This, in turn, enhances the NO$_3^-$RR activity of Janus Cu@Ni/C for the conversion of NO$_3^-$ into NH$_3$.

CONCLUSIONS

In our study, we provide valuable insights into the process of optimizing catalysts into a phase-separated structure for enhancing their performance against the NO$_3^-$RR by a phase-dependent mechanism. By conducting this research, we shed light on the factors and parameters that can be adjusted to improve the catalytic activity by constructing two active sites adjacent to each other. While acknowledging that certain structural features of the Cu@Ni catalyst with different metal ratios remain unexplored and these variations may also lead to different catalytic activities. We believe that the tandem cooperation between adjacent active sites on the Cu-rich and Ni-rich phases, as described in our mechanistic study with a ratio of 50:50, offers insights for the design of multicomponent heterogeneous catalysts. Understanding and providing alternative explanations on how to fine-tune catalysts is crucial because it can prompt more efficient and effective systems (rather than a homogeneous alloy) for reducing NO$_3^-$ into valuable product such NH$_3$, ultimately contributing to cleaner and more sustainable energy technologies and environmental protection.

ASSOCIATED CONTENT

Supporting Information
The Supporting Information is available free of charge at https://pubs.acs.org/doi/10.1021/acscatal.4c00479.

XRD patterns; XPS spectra; electrocatalytic performance data over catalysts of Cu$_{50}$Ni$_{50}$-Janus/C, Cu$_{50}$Ni$_{50}$-SSA/C, Cu$_{50}$Ni$_{50}$-Mix/C, Cu/C, and Ni/C; TEM images with particle size distribution; EPR spectra; EXAFS spectra; in situ FTIR spectra; and their quantitative analysis (PDF)

AUTHOR INFORMATION

Corresponding Authors
Yao-Yin Lou − CAS Key Laboratory of Urban Pollutant Conversion, Institute of Urban Environment, Chinese Academy of Sciences, Xiamen 361021, P. R. China; State Key Laboratory of Physical Chemistry of Solid Surfaces, Department of Chemistry, College of Chemistry and Chemical Engineering, Xiamen University, Xiamen 361005, China; orcid.org/0000-0002-2782-2130; Email: yylou@iue.ac.cn
Xiaoyang Huang − State Key Laboratory of Physical Chemistry of Solid Surfaces, Department of Chemistry, College of Chemistry and Chemical Engineering, Xiamen University, Xiamen 361005, China; Center of Advanced Electrochemical Energy, Institute of Advanced Interdisciplinary Studies, Chongqing University, Chongqing 400044, China; Cardiff Catalysis Institute, School of Chemistry, Cardiff University, Cardiff, Wales CF10 3AT, U.K.; orcid.org/0000-0002-7221-2075; Email: HuangX17@cardiff.ac.uk

Shi-Gang Sun − State Key Laboratory of Physical Chemistry of Solid Surfaces, Department of Chemistry, College of Chemistry and Chemical Engineering, Xiamen University, Xiamen 361005, China; Center of Advanced Electrochemical Energy, Institute of Advanced Interdisciplinary Studies, Chongqing University, Chongqing 400044, China; orcid.org/0000-0003-2327-4090; Email: sgsun@xmu.edu.cn

Authors
Qi-Zheng Zheng − State Key Laboratory of Physical Chemistry of Solid Surfaces, Department of Chemistry, College of Chemistry and Chemical Engineering, Xiamen University, Xiamen 361005, China; orcid.org/0000-0002-9508-5822
Shi-Yuan Zhou − State Key Laboratory of Physical Chemistry of Solid Surfaces, Department of Chemistry, College of Chemistry and Chemical Engineering, Xiamen University, Xiamen 361005, China
Jia-Yi Fang − State Key Laboratory of Physical Chemistry of Solid Surfaces, Department of Chemistry, College of Chemistry and Chemical Engineering, Xiamen University, Xiamen 361005, China
Ouardia Akdim − Cardiff Catalysis Institute, School of Chemistry, Cardiff University, Cardiff, Wales CF10 3AT, U.K.; orcid.org/0000-0003-3915-7681
Xing-Yu Ding − State Key Laboratory of Physical Chemistry of Solid Surfaces, Department of Chemistry, College of Chemistry and Chemical Engineering, Xiamen University, Xiamen 361005, China
Rena Oh − Department of Materials Science and Engineering and Research Institute of Advanced Materials, Seoul National University, Seoul 08826, Republic of Korea; orcid.org/0000-0001-9729-0398
Gyeong-Su Park − Institute of Next-Generation Semiconductor Convergence Technology, Daegu Gyeongbuk Institute of Science and Technology (DGIST), Daegu 42988, Republic of Korea; orcid.org/0000-0002-5820-8280

Complete contact information is available at:
https://pubs.acs.org/10.1021/acscatal.4c00479

Author Contributions
Y.Y.L. and Q.Z.Z. contributed equally to this work. Y.Y.L., X.Y.H., and S.G.S. contributed to the design of the study; Y.Y.L., S.Y.Z., J.Y.F., X.Y.H., and X.Y.D. conducted experiments and data analysis. Q.Z.Z. conducted the DFT calculations. Y.Y.L., O.A., and X.Y.H. conceived the mechanism; Y.Y.L., R.O., G.P., and S.S.G. provided technical support, conceptual advice, and result interpretation. Y.Y.L., X.Y.H., O.A., and R.O. wrote the manuscript and the Supporting Information. All authors commented on- and amended both documents. All authors discussed and contributed to the work.

Notes
The authors declare no competing financial interest.

ACKNOWLEDGMENTS

Planck-Cardiff Centre for their input on the discussion of phase-separated catalyst synthesis.

■ REFERENCES

(1) Huang, X.; Akdim, O.; Douthwaite, M.; Wang, K.; Zhao, L.; Lewis, R. J.; Pattisson, S.; Daniel, I. T.; Miedziak, P. J.; Shaw, G.; Morgan, D. J.; Althahban, S. M.; Davies, T. E.; He, Q.; Wang, F.; Fu, J.; Bethell, D.; McIntosh, S.; Kiely, C. J.; Hutchings, G. J. Au-Pd separation enhances bimetallic catalysis of alcohol oxidation. *Nature* **2022**, *603* (7900), 271−275.

(2) Rai, R. K.; Tyagi, D.; Gupta, K.; Singh, S. K. Activated nanostructured bimetallic catalysts for C-C coupling reactions: recent progress. *Catal. Sci. Technol.* **2016**, *6* (10), 3341−3361.

(3) Wang, Y.; Xu, A.; Wang, Z.; Huang, L.; Li, J.; Li, F.; Wicks, J.; Luo, M.; Nam, D.-H.; Tan, C.-S.; Ding, Y.; Wu, J.; Lum, Y.; Dinh, C.-T.; Sinton, D.; Zheng, G.; Sargent, E. H. Enhanced Nitrate-to-Ammonia Activity on Copper-Nickel Alloys via Tuning of Intermediate Adsorption. *J. Am. Chem. Soc.* **2020**, *142* (12), 5702−5708.

(4) He, W.; Zhang, J.; Dieckhöfer, S.; Varhade, S.; Brix, A. C.; Lielpetere, A.; Seisel, S.; Junqueira, J. R.; Schuhmann, W. Splicing the active phases of copper/cobalt-based catalysts achieves high-rate tandem electroreduction of nitrate to ammonia. *Nat. Commun.* **2022**, *13* (1), 1−13.

(5) Ma, Y. B.; Yu, J. L.; Sun, M. Z.; Chen, B.; Zhou, X. C.; Ye, C. L.; Guan, Z. Q.; Guo, W. H.; Wang, G.; Lu, S. Y.; Xia, D. S.; Wang, Y. H.; He, Z.; Zheng, L.; Yun, Q. B.; Wang, L. Q.; Zhou, J. W.; Lu, P. Y.; Yin, J. W.; Zhao, Y. F.; Luo, Z. B.; Zhai, L.; Liao, L. W.; Zhu, Z. L.; Ye, R. Q.; Chen, Y.; Lu, Y.; Xi, S. B.; Huang, B. L.; Lee, C. S.; Fan, Z. X. Confined Growth of Silver-Copper Janus Nanostructures with {100} Facets for Highly Selective Tandem Electrocatalytic Carbon Dioxide Reduction. *Adv. Mater.* **2022**, *34* (19), 2110607.

(6) Wang, J.; Li, Z.; Dong, C.; Feng, Y.; Yang, J.; Liu, H.; Du, X. Silver/Copper Interface for Relay Electroreduction of Carbon Dioxide to Ethylene. *ACS Appl. Mater. Interfaces* **2019**, *11* (3), 2763−2767.

(7) Zheng, Y.; Zhang, J.; Ma, Z.; Zhang, G.; Zhang, H.; Fu, X.; Ma, Y.; Liu, F.; Liu, M.; Huang, H. Seeded Growth of Gold-Copper Janus Nanostructures as a Tandem Catalyst for Efficient Electroreduction of CO_2 to C_{2+} Products. *Small* **2022**, *18* (19), 2201695.

(8) Ye, S.; Chen, Z.; Zhang, G.; Chen, W.; Peng, C.; Yang, X.; Zheng, L.; Li, Y.; Ren, X.; Cao, H.; Xue, D.; Qiu, J.; Zhang, Q.; Liu, J. Elucidating the activity, mechanism and application of selective electrosynthesis of ammonia from nitrate on cobalt phosphide. *Energy Environ. Sci.* **2022**, *15* (2), 760−770.

(9) Liu, X.; Elgowainy, A.; Wang, M. Life cycle energy use and greenhouse gas emissions of ammonia production from renewable resources and industrial by-products. *Green Chem.* **2020**, *22* (17), 5751−5761.

(10) Smith, C.; Hill, A. K.; Torrente-Murciano, L. Current and future role of Haber-Bosch ammonia in a carbon-free energy landscape. *Energy Environ. Sci.* **2020**, *13* (2), 331−344.

(11) van Langevelde, P. H.; Katsounaros, I.; Koper, M. T. M. Electrocatalytic Nitrate Reduction for Sustainable Ammonia Production. *Joule* **2021**, *5* (2), 290−294.

(12) Zheng, W. X.; Zhu, L. Y.; Yan, Z.; Lin, Z. C.; Lei, Z. C.; Zhang, Y. F.; Xu, H. L.; Dang, Z.; Wei, C. H.; Feng, C. H. Self-Activated Ni Cathode for Electrocatalytic Nitrate Reduction to Ammonia: From Fundamentals to Scale-Up for Treatment of Industrial Wastewater. *Environ. Sci. Technol.* **2021**, *55* (19), 13231−13243.

(13) Reyter, D.; Bélanger, D.; Roué, L. Optimization of the cathode material for nitrate removal by a paired electrolysis process. *J. Hazard. Mater.* **2011**, *192* (2), 507−513.

(14) Han, S.; Li, H.; Li, T.; Chen, F.; Yang, R.; Yu, Y.; Zhang, B. Ultralow overpotential nitrate reduction to ammonia via a three-step relay mechanism. *Nat. Catal.* **2023**, *6*, 402−414.

(15) Li, P.; Li, R.; Liu, Y.; Xie, M.; Jin, Z.; Yu, G. Pulsed Nitrate-to-Ammonia Electroreduction Facilitated by Tandem Catalysis of Nitrite Intermediates. *J. Am. Chem. Soc.* **2023**, *145* (11), 6471−6479.

(16) Lim, J.; Liu, C.-Y.; Park, J.; Liu, Y.-H.; Senftle, T. P.; Lee, S. W.; Hatzell, M. C. Structure Sensitivity of Pd Facets for Enhanced Electrochemical Nitrate Reduction to Ammonia. *ACS Catal.* **2021**, *11* (12), 7568−7577.

(17) Wang, Y.; Zhou, W.; Jia, R.; Yu, Y.; Zhang, B. Unveiling the activity origin of a copper-based electrocatalyst for selective nitrate reduction to ammonia. *Angew. Chem., Int. Ed.* **2020**, *59* (13), 5350−5354.

(18) Liu, L.; Zheng, S.-J.; Chen, H.; Cai, J.; Zang, S.-Q. Tandem Nitrate-to-Ammonia Conversion on Atomically Precise Silver Nano-cluster/MXene Electrocatalyst. *Angew. Chem. Int. Ed.* **2024**, *63* (8), No. e202316910.

(19) Fu, Y.; Wang, S.; Wang, Y.; Wei, P.; Shao, J.; Liu, T.; Wang, G.; Bao, X. Enhancing Electrochemical Nitrate Reduction to Ammonia over Cu Nanosheets via Facet Tandem Catalysis. *Angew. Chem.* **2023**, *135* (26), No. e202303327.

(20) Feng, J.; Zhang, L.; Liu, S.; Xu, L.; Ma, X.; Tan, X.; Wu, L.; Qian, Q.; Wu, T.; Zhang, J.; Sun, X.; Han, B. Modulating adsorbed hydrogen drives electrochemical CO_2-to-C_2 products. *Nat. Commun.* **2023**, *14* (1), 4615.

(21) Fang, J.-Y.; Zheng, Q.-Z.; Lou, Y.-Y.; Zhao, K.-M.; Hu, S.-N.; Li, G.; Akdim, O.; Huang, X.-Y.; Sun, S.-G. Ampere-level current density ammonia electrochemical synthesis using CuCo nanosheets simulating nitrite reductase bifunctional nature. *Nat. Commun.* **2022**, *13* (1), 7899.

(22) Liu, J.-X.; Richards, D.; Singh, N.; Goldsmith, B. R. Activity and Selectivity Trends in Electrocatalytic Nitrate Reduction on Transition Metals. *ACS Catal.* **2019**, *9* (8), 7052−7064.

(23) Jung, W.; Jeong, J.; Chae, Y.; Lee, W. H.; Ko, Y.-J.; Chae, K. H.; Oh, H.-s.; Lee, U.; Lee, D. K.; Min, B. K.; Shin, H.; Hwang, Y. J.; Won, D. H. Synergistic bimetallic CuPd oxide alloy electrocatalyst for ammonia production from the electrochemical nitrate reaction. *J. Mater. Chem. A* **2022**, *10* (44), 23760−23769.

(24) Li, J.; Zhan, G.; Yang, J.; Quan, F.; Mao, C.; Liu, Y.; Wang, B.; Lei, F.; Li, L.; Chan, A. W. M.; Xu, L.; Shi, Y.; Du, Y.; Hao, W.; Wong, P. K.; Wang, J.; Dou, S.-X.; Zhang, L.; Yu, J. C. Efficient Ammonia Electrosynthesis from Nitrate on Strained Ruthenium Nanoclusters. *J. Am. Chem. Soc.* **2020**, *142* (15), 7036−7046.

(25) Chen, F.-Y.; Wu, Z.-Y.; Gupta, S.; Rivera, D. J.; Lambeets, S.; Pecaut, S.; Kim, J. Y. T.; Zhu, P.; Finfrock, Y. Z.; Meira, D. M.; King, G.; Gao, G.; Xu, W.; Cullen, D. A.; Zhou, H.; Han, Y.; Perea, D. E.; Muhich, C. L.; Wang, H. Efficient conversion of low-concentration nitrate sources into ammonia on a Ru-dispersed Cu nanowire electrocatalyst. *Nat. Nanotechnol.* **2022**, *17* (7), 759−767.

(26) Simpson, B. K.; Johnson, D. C. Electrocatalysis of Nitrate Reduction at Copper-Nickel Alloy Electrodes in Acidic Media. *Electroanalysis* **2004**, *16* (7), 532−538.

(27) Tian, X.; Zhao, P.; Sheng, W. Hydrogen Evolution and Oxidation: Mechanistic Studies and Material Advances. *Adv. Mater.* **2019**, *31* (31), 1808066.

(28) Nakaya, Y.; Furukawa, S. Catalysis of Alloys: Classification, Principles, and Design for a Variety of Materials and Reactions. *Chem. Rev.* **2023**, *123* (9), 5859−5947.

(29) Liu, R.; Zhao, H.; Zhao, X.; He, Z.; Lai, Y.; Shan, W.; Bekana, D.; Li, G.; Liu, J. Defect Sites in Ultrathin Pd Nanowires Facilitate the Highly Efficient Electrochemical Hydrodechlorination of Pollutants by H*ads. *Environ. Sci. Technol.* **2018**, *52* (17), 9992−10002.

(30) Yin, H.; Chen, Z.; Xiong, S.; Chen, J.; Wang, C.; Wang, R.; Kuwahara, Y.; Luo, J.; Yamashita, H.; Peng, Y.; Li, J. Alloying effect-induced electron polarization drives nitrate electroreduction to ammonia. *Chem Catal.* **2021**, *1* (5), 1088−1103.

(31) Bae, S.-E.; Stewart, K. L.; Gewirth, A. A. Nitrate Adsorption and Reduction on Cu(100) in Acidic Solution. *J. Am. Chem. Soc.* **2007**, *129* (33), 10171−10180.

(32) Molodkina, E. B.; Ehrenburg, M. R.; Polukarov, Y. M.; Danilov, A. I.; Souza-Garcia, J.; Feliu, J. M. Electroreduction of nitrate ions on Pt(111) electrodes modified by copper adatoms. *Electrochim. Acta* **2010**, *56* (1), 154−165.

(33) de Groot, M. T.; Koper, M. T. M. The influence of nitrate concentration and acidity on the electrocatalytic reduction of nitrate on platinum. *J. Electroanal. Chem.* **2004**, *562* (1), 81−94.

(34) Wang, Y.; Li, H.; Zhou, W.; Zhang, X.; Zhang, B.; Yu, Y. Structurally Disordered RuO_2 Nanosheets with Rich Oxygen Vacancies for Enhanced Nitrate Electroreduction to Ammonia. *Angew. Chem., Int. Ed.* **2022**, *61* (19), No. e202202604.

(35) Zhou, J.; Han, S.; Yang, R.; Li, T.; Li, W.; Wang, Y.; Yu, Y.; Zhang, B. Linear Adsorption Enables NO Selective Electroreduction to Hydroxylamine on Single Co Sites. *Angew. Chem.* **2023**, *135*, No. e202305184.

(36) Rodes, A.; Climent, V.; Orts, J. M.; Pérez, J.; Aldaz, A. Nitric oxide adsorption at Pt(100) electrode surfaces. *Electrochim. Acta* **1998**, *44* (6−7), 1077−1090.

(37) Yan, Y.-G.; Huang, B.-B.; Wang, J.-Y.; Wang, H.-F.; Cai, W.-B. In situ surface-enhanced IR absorption spectroscopy on the adsorption and reduction of nitric oxide at ruthenium electrode. *J. Catal.* **2007**, *249* (2), 311−317.

(38) Figueiredo, M. C.; Souza-Garcia, J.; Climent, V.; Feliu, J. M. Nitrate reduction on Pt(111) surfaces modified by Bi adatoms. *Electrochem. Commun.* **2009**, *11* (9), 1760−1763.

(39) Gootzen, J. F. E.; van Hardeveld, R. M.; Visscher, W.; van Santen, R. A.; van Veen, J. A. R. The study of NO adsorbate layers on platinized platinum in the liquid phase with cyclic voltammetry, DEMS and FTIRS. *Recl. Trav. Chim. Pays-Bas* **1996**, *115* (11−12), 480−485.

(40) Álvarez, B.; Rodes, A.; Pérez, J. M.; Feliu, J. M.; Rodríguez, J. L.; Pastor, E. Spectroscopic Study of the Nitric Oxide Adlayers Formed from Nitrous Acid Solutions on Palladium-Covered Platinum Single-Crystal Electrodes. *Langmuir* **2000**, *16* (10), 4695−4705.

(41) Nakata, K.; Kayama, Y.; Shimazu, K.; Yamakata, A.; Ye, S.; Osawa, M. Surface-enhanced infrared absorption spectroscopic studies of adsorbed nitrate, nitric oxide, and related compounds 2: Nitrate ion adsorption at a platinum electrode. *Langmuir* **2008**, *24* (8), 4358−4363.

(42) Liu, Y.-X.; Zhang, W.-Y.; Han, G.-K.; Zhou, Y.-W.; Li, L.-F.; Kang, C.; Kong, F.-P.; Gao, Y.-Z.; Du, C.-Y.; Wang, J.-J.; Ma, Y.-L.; Du, L.; Cai, W.-B.; Yin, G.-P. Deactivation and regeneration of a benchmark Pt/C catalyst toward oxygen reduction reaction in the presence of poisonous SO_2 and NO. *Catal. Sci. Technol.* **2022**, *12* (9), 2929−2934.

(43) Ma, M.; Yi-Jin, W.; Wang, J. Y.; Li, Q. X.; Cai, W. B. A study of NO adducts of iron protoporphyrin IX adlayer on au electrode with in Situ ATR-FTIR spectroscopy. *J. Phys. Chem. C* **2007**, *111* (24), 8649−8654.

(44) Wei, Z.-W.; Wang, H.-J.; Zhang, C.; Xu, K.; Lu, X.-L.; Lu, T.-B. Reversed Charge Transfer and Enhanced Hydrogen Spillover in Platinum Nanoclusters Anchored on Titanium Oxide with Rich Oxygen Vacancies Boost Hydrogen Evolution Reaction. *Angew. Chem., Int. Ed.* **2021**, *60* (30), 16622−16627.

(45) Karim, W.; Spreafico, C.; Kleibert, A.; Gobrecht, J.; VandeVondele, J.; Ekinci, Y.; van Bokhoven, J. A. Catalyst support effects on hydrogen spillover. *Nature* **2017**, *541* (7635), 68−71.

(46) Chen, L.; Cooper, A. C.; Pez, G. P.; Cheng, H. Mechanistic Study on Hydrogen Spillover onto Graphitic Carbon Materials. *J. Phys. Chem. C* **2007**, *111* (51), 18995−19000.